Journal of the Mechanical Behavior of Biomedical Materials 94 (2019) 155–163

Contents lists available at ScienceDirect

Journal of the Mechanical Behavior of Biomedical Materials

journal homepage: www.elsevier.com/locate/jmbbm

Mechanical properties of *Chamelea gallina* shells at different latitudes

Roberto Guarino[a], Stefano Goffredo[b,c], Giuseppe Falini[d], Nicola Maria Pugno[a,e,f,*]

[a] Laboratory of Bio-Inspired & Graphene Nanomechanics, Department of Civil, Environmental and Mechanical Engineering, University of Trento, Via Mesiano 77, 38123 Trento, Italy
[b] Marine Science Group, Department of Biological, Geological and Environmental Sciences, University of Bologna, Via F. Selmi 3, 40126 Bologna, Italy
[c] Laboratory of Marine Biology and Fisheries at Fano, Department of Biological, Geological and Environmental Sciences, University of Bologna, Viale Adriatico 1/N, 61032 Fano, Italy
[d] Department of Chemistry 'Giacomo Ciamician', University of Bologna, Via F. Selmi 2, 40126 Bologna, Italy
[e] Ket Lab, Edoardo Amaldi Foundation, Via del Politecnico snc, 00133 Rome, Italy
[f] School of Engineering and Materials Science, Queen Mary University of London, Mile End Road, E1-4NS London, United Kingdom

ARTICLE INFO

Keywords:
Clam shells
Abiotic factors
Aragonite
Analytical modelling
Fracture

ABSTRACT

In this work we evaluate the mechanical properties of *Chamelea gallina* shells, collected at various locations in the Adriatic Sea, through compression tests. We present an analytical model for the extraction of the material Young's modulus and ultimate strength, based on the approximation of the valves with a simpler geometry. The effect of porosity and the computation of the energy dissipated at fracture are also discussed. Results show a dependence of the mechanical performance on the location at which the samples were collected, i.e. latitude, and thus the environmental factors can affect the rigidity, strength and toughness of the shells. These findings integrate preliminary results published in a previous work.

1. Introduction

It is well known that organisms are able to modify their development and their gene-expression patterns in response to environmental parameters, such as temperature, or to biotic factors, such as food availability or density of predators (Gilbert, 2001). Specifically, the adaptation or acclimation to changing environmental conditions is of extreme interest in developmental biology, also considering the alarming climatic changes of the last decades. Phenotype plasticity is the ability of organisms to produce a range of relatively fit phenotypes, by altering morphology, behaviour or rate of biological activity in response to variations in environmental conditions (DeWitt and Scheiner, 2004).

Calcifying marine organisms, such as corals and molluscs, are among the most susceptible species to changing abiotic factors, since they usually show morphological variations in their skeleton or shell in response to changes in external environmental conditions, e.g. temperature and pH (Watson et al., 2012; Melatunan et al., 2013). These organisms usually employ calcium carbonate ($CaCO_3$) as structural material, which is synthetised through a cascade of biochemical processes referred as biomineralization. In mollusc shells, $CaCO_3$ is found in the form of aragonite and/or calcite, which represent the basic microstructural constituents and are generally assembled within an organic matrix. When co-present, these two polymorphs are differently localized and never mixed in a solid solution (Lowenstam and Weiner, 1989).

The commercial clam *Chamelea gallina* is a common bivalve of the Mediterranean Sea and has a great importance for the fishery in several countries. For instance, the annual yield in Italy is currently about 20,000 metric tons (Romanelli et al., 2008), but it has reached 100,000 metric tons in the late 1970s. The over-exploitation of the resource, therefore, has posed recently growing concerns for the survival of these bivalve communities. In fact, unexpected annual fluctuations in stock abundance, periodic recruitment failures and irregular mortality events can threaten the biological and economic sustainability of this fishery.

The study of the effects of the changing environmental factors on *C. gallina* growth and characteristics, therefore, is of increasing interest also from an economic point of view. In a previous work, samples of *C. gallina* shells were collected at different latitudes in the Adriatic Sea, with the objective to evaluate the effects of solar radiation and sea temperature on the physical properties (e.g. geometry) of the shells. The authors found that the variation of the shell properties along the latitudinal gradient "could be the outcome of phenotypic plasticity, or a genetic adaptation of the populations subjected to different

* Corresponding author at: Laboratory of Bio-Inspired & Graphene Nanomechanics, Department of Civil, Environmental and Mechanical Engineering, University of Trento, Via Mesiano 77, 38123 Trento, Italy.
E-mail address: nicola.pugno@unitn.it (N.M. Pugno).

https://doi.org/10.1016/j.jmbbm.2019.02.032
Received 13 December 2018; Received in revised form 21 February 2019; Accepted 28 February 2019
Available online 01 March 2019
1751-6161/

environmental parameters" (Gizzi et al., 2016). These parameters could directly affect the shell morphology and growth (Ramón and Richardson, 1992; Moschino and Marin, 2006; Matozzo and Marin, 2011), or indirectly, e.g. impacting the nutrient concentration and/or predator density.

The present paper is focused on a systematic investigation of the mechanical properties of *C. gallina* shells through compression tests. Starting from the classical theory of shallow spherical shells loaded at the centre, we consider an equivalent spherical geometry and extract the Young's modulus and the ultimate strength of the valves. The effect of the geometry, and specifically the thickness of the shells, on the macroscopic properties is discussed, as well as the influence of porosity. The toughness modulus and the fracture energy of the shells are also quantified from the experimental load-displacement curves. Additionally, we present some Scanning Electron Microscopy (SEM) and X-Ray Diffraction (XRD) analyses of the shells, in order to provide an overview of their main composition and microstructural morphology.

2. Experimental tests

2.1. Description of the shells and locations

The clam *Chamelea gallina* (Linnaeus 1758) is a common infaunal bivalve in the family Veneridae of the Mediterranean Sea, where it inhabits well-sorted fine sand biocoenosis at 3–7 m depth (Ramón and Richardson, 1992).

A valve of the *C. gallina* shell appears as a hemi-ellipsoid object, as shown in Fig. 1. Its external surface shows a roughness generated by the growth rings, while the internal surface is smooth. In general, the shell thickness, intended as the average distance between the internal and the external surface of the valve, is not constant and increases from the umbo to the periphery. In addition, the shell has usually a homogeneous chemical composition and is made of $CaCO_3$ in the form of aragonite.

C. gallina samples have been collected at various locations with different latitudes in the Adriatic Sea (see Supplementary Fig. 1). In Table 1 we list the two main environmental parameters of the selected locations, i.e. the mean annual solar radiation level and the sea surface temperature, which have been demonstrated to have an impact on the shell biometry and growth, together with the main geometrical parameters used later. The number of samples denotes the number of investigated clams, thus every data reported later is related to the average between the left and the right valve of each clam. The biometric parameters of dry valves have been measured with a pair of calipers (± 0.05 mm), while the volume and average porosity of each valve have been extracted by means of the buoyant weight technique, through a density determination kit Ohaus Explorer Pro balance (± 0.1 mg; Ohaus Corporation, Pine Brook - NJ, United States of America). For all the other details concerning abiotic environmental factors and the measurement of biometric parameters, the reader is referred to the previous work on *C. gallina* shells (Gizzi et al., 2016).

2.2. Scanning Electron Microscopy (SEM)

SEM observations were carried on the transversal valve sections obtained using a steel saw. Each section was etched with an acetic acid solution (1% v/v) for 1 min to remove debris and artefacts from cutting. Samples were coated with a gold layer (5 nm) and analysed with a SEM Hitachi S4000 (Hitachi High-Technologies Europe GmbH, Germany).

As highlighted in Fig. 2, the SEM observations showed that the microstructure of *C. gallina* shell contains two main layers, according to what observed in most Venerids (Popov, 1986). The boundary region between the two layers (Fig. 2a) shows fractures given by the compression tests. These fractures originate from the inner layer, while the outer layer remains nearly unaltered. The pristine sample, instead, shows a continuity of bond between the two layers. In the external layer (Fig. 2b) compound prisms are observed. They are formed by an open aggregation of grains having irregular shapes and highly interconnected (Fig. 2c). The inner layer is homogeneous and is formed of compact granules which give a spherulitic appearance (Fig. 2d,e). Among these grains, having a size around 1 μm, layers of organic material are dispersed. The boundary region between the two layers, when observed at high magnifications (Fig. 2g,h) shows a low regularity in the weaving of the particles that show larger dimensions than those observed in the external and internal state.

The lamellar multiscale structure present in *C. gallina* shells is commonly found in nacre (see, e.g., Sun and Bhushan, 2012) and in other seashells (Li et al., 2004, 2013). Also the shells of Pectinidae present a complex fracture surface, in which it is possible to identify different layers (Li and Nardi, 2004), namely an inner and an outer part as in our case. Interestingly, the observed spherulitic microstructure (Fig. 2d,e), in addition, is found very similar in nacre and conch shells treated at high temperature, where the platelets essentially assume a quasi-spherical shape (Huang and Li, 2009; Li et al., 2015). The macroscopic mechanical performance of the valves are believed to be strongly dependent on the size of the largest microstructural units (Taylor and Layman, 1972), while the organic matrix content essentially influences the Young's modulus and the fracture properties. Specifically, the organic matrix is basically made of biopolymers that have the capabilities to strengthen themselves during deformation, as demonstrated experimentally (Xu and Li, 2011). Thus the macroscopic mechanical behaviour derives from a complex interplay of several factors, including platelets/lamellae dimensions and shapes, biopolymer content and thus the shear strength of the interfaces. The extensibility of the interfaces, i.e. their ability to sustain deformation, is fundamental for the extreme toughness observed in nacre-like materials (Barthelat et al., 2016).

The presence of two different layers confers to the shell anisotropic mechanical properties, as determined experimentally in previous works

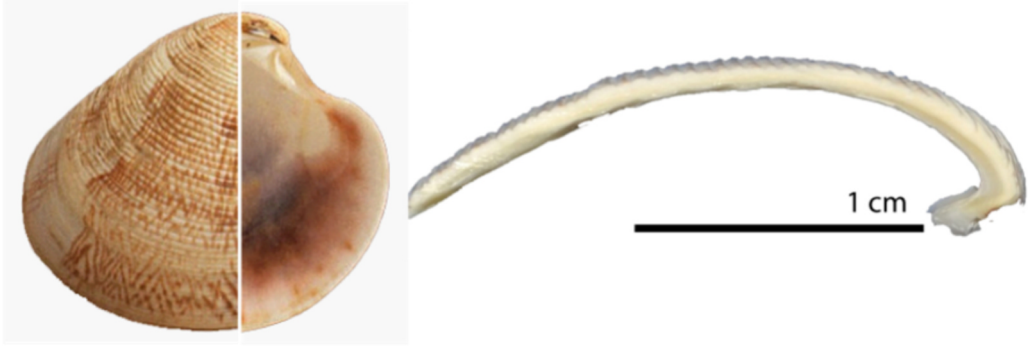

Fig. 1. External and internal view (left) and cross section (right) of a valve of *C. gallina*.

Table 1
Location characteristics with average value and standard deviation of the annual solar radiation and sea surface temperature, average value and standard deviation of the main geometrical parameters and number of the investigated samples, ordered by decreasing latitudes.
Source: Adapted from Gizzi et al. (2016).

Location characteristics				Main biometric parameters				Number of samples
Acronym	**Latitude** (°)	**Solar radiation** (W/m^2)	**Sea surface temperature** (°C)	**Max Feret diameter** (mm)	**Min Feret diameter** (mm)	**Height at shell centre** (mm)	**Average shell thickness** (mm)	
"MO"	45.7	172.4 ± 2.5	17.90 ± 0.19	26.7 ± 1.3	22.3 ± 0.9	7.4 ± 0.4	1.6 ± 0.2	27
"CH"	45.2	160.8 ± 2.5	16.47 ± 0.19	26.2 ± 1.3	21.5 ± 1.1	6.4 ± 0.3	1.3 ± 0.2	27
"GR"	44.8	163.8 ± 2.6	16.54 ± 0.19	26.2 ± 1.6	21.5 ± 1.4	6.8 ± 0.4	1.3 ± 0.2	27
"CE"	44.2	165.2 ± 2.5	17.05 ± 0.20	26.2 ± 1.5	21.2 ± 1.2	6.4 ± 0.5	1.1 ± 0.1	31
"SB"	43.1	180.4 ± 2.6	18.60 ± 0.17	26.2 ± 1.2	21.6 ± 0.7	6.4 ± 0.4	1.2 ± 0.1	27
"CA"	41.9	180.4 ± 2.6	18.60 ± 0.17	26.0 ± 1.6	21.0 ± 1.2	6.0 ± 0.4	1.1 ± 0.1	27

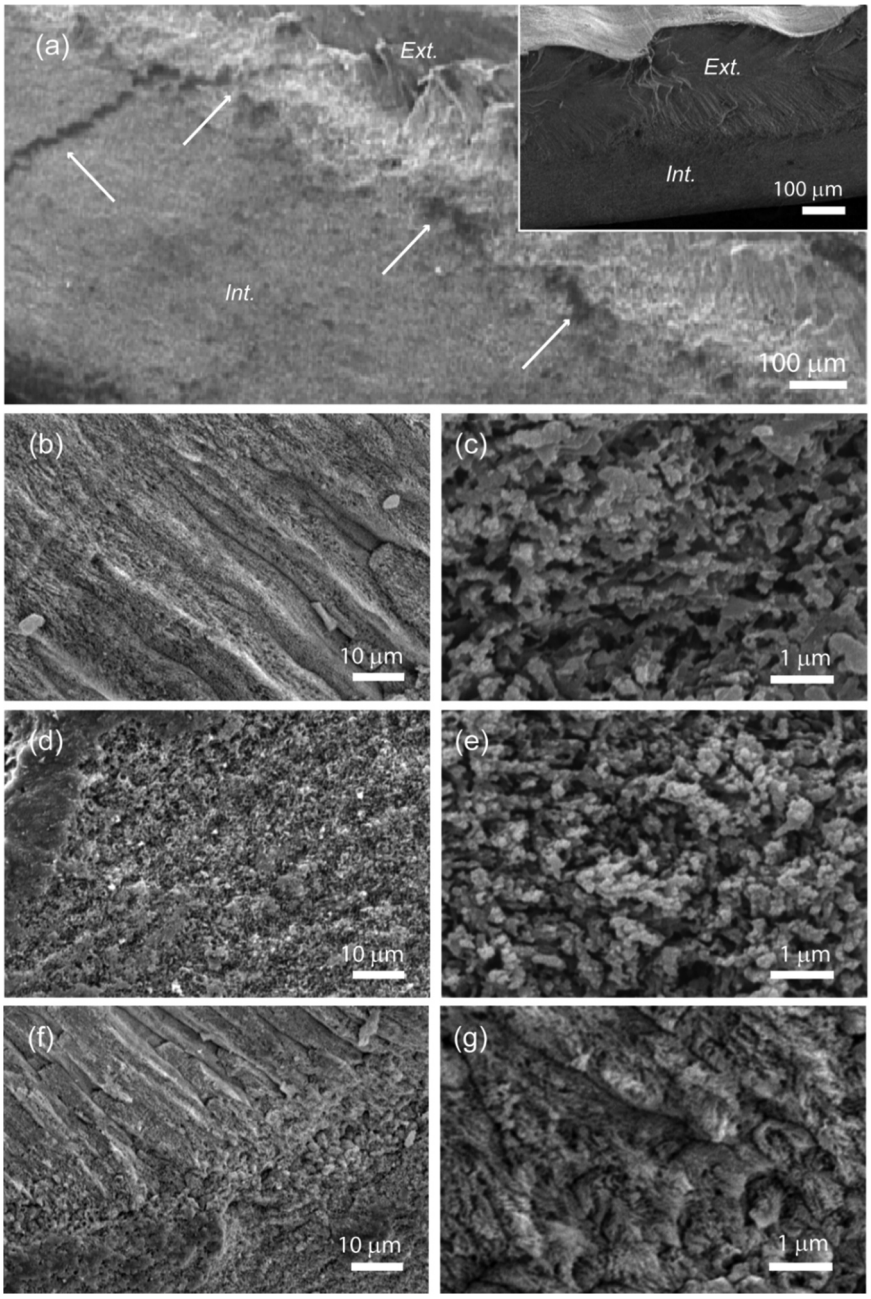

Fig. 2. SEM images of the cross section of a valve of *C. gallina*. **(a)** A low-magnification image of a region close to the umbo from a valve that was compressed without fracture. The outer (Ext.) and inner (Int.) layers are observable. The arrows indicate the region were fractures were observed. Inset: cross section of a pristine sample. **(b,c)** Images of the outer layer at low and high magnification, respectively. **(d,e)** Images of the inner layer at low and high magnification, respectively. **(f,g)** Images of the outer-inner junction region at low and high magnification, respectively.

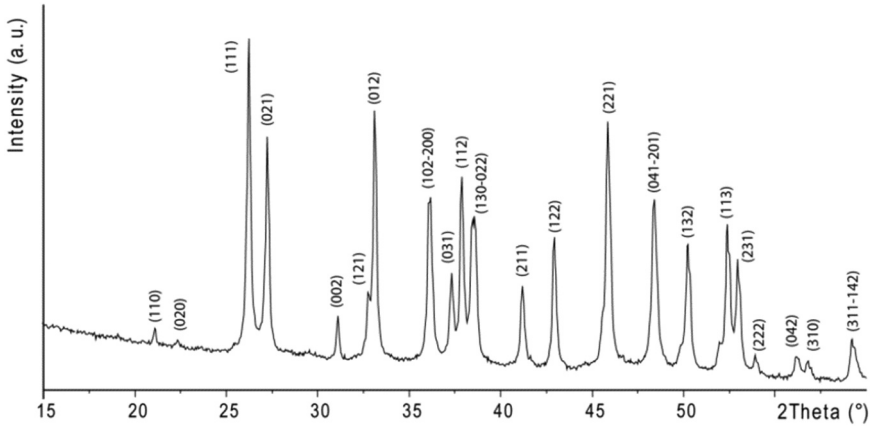

Fig. 3. XRD pattern of a sample of ground shell. The diffraction peaks were indexed according to the reference JCPDS card 41-1475 (Keller et al., 1989).

(Bignardi et al., 2010) and as we are going to quantify later in terms of toughness modulus and fracture energy.

2.3. X-Ray Diffraction (XRD)

XRD analysis was performed after preparing a compact layer of powdered sample in a silica background signal free holder. Diffraction patterns for each sample were collected using an X'Celerator detector fitted on a PANalytical X'Pert Pro diffractometer (Malvern Panalytical Ltd, United Kingdom), using Cu-Kα radiation generated at 40 kV and 40 mA. Data were collected within the 2θ range from 15° to 60° with a step size of 0.02° and a counting time of 1200 s. Fixed anti-scatter and divergence slits of 1/16° were used with a 10 mm beam mask and all scans were carried out in "continuous" mode.

The diffraction pattern is shown in Fig. 3, where all the diffraction peaks are indexed according to the structure of aragonite (Pilati et al., 1998).

2.4. Compression tests

The compression tests for the evaluation of the mechanical properties of the *C. gallina* shells were carried out in displacement control using an Instron universal testing machine (Illinois Tool Works Inc., Norwood - MA, United States of America) equipped with a 1 kN load cell, as shown in Fig. 4. The load using a 3 cm diameter compression platen moved at a constant downward speed of 0.5 mm min^{-1}. Each valve was treated with a 5% sodium hypochlorite solution for three days, in order to completely remove any trace of external organic tissue, and with a 1 M sodium hydroxide solution for one day, for the hydrolyzation of the residual proteic materials from the shell surface. Samples were then rinsed with distilled water and dried at room temperature for one day. We tested dry samples because the mechanical response of the shells could be influenced also by their water content, which is believed to be responsible for the viscoelastic behaviour (Mohanty et al., 2006), but this investigation is beyond the scope of the present work.

A typical experimental load-displacement curve is plotted in Fig. 5, where it is possible to distinguish two main parts: the first quasi-linear elastic segment, until the maximum load P_{max} is reached, and the subsequent fracture, characterised by irregular rises and drops of the load as the crack grows.

This mechanical behaviour has already been observed and widely studied in the literature (see, e.g., Barthelat et al., 2009; Mayer, 2017) and is typical of natural and artificial laminate composite materials. As anticipated above, the complex fracture behaviour of *C. gallina* shells, emerging from Fig. 5, can be attributed to their multiscale architecture, which allows different energy-dissipating mechanisms. As observed also in other seashells (Espinosa et al., 2011; Ji et al., 2017) and nacre-like materials (Kakisawa and Sumitomo, 2011; Huang and Li, 2013; Yuan et al., 2016), on one side, one of the core mechanisms is the deformation of the aragonite micro-platelets and their sliding, closely related to the shear strength of the interfaces; while on the other side, the crack propagation between the lamellae (and inside the lamellae at higher loads), which drive the crack path towards the regions with larger stress intensities.

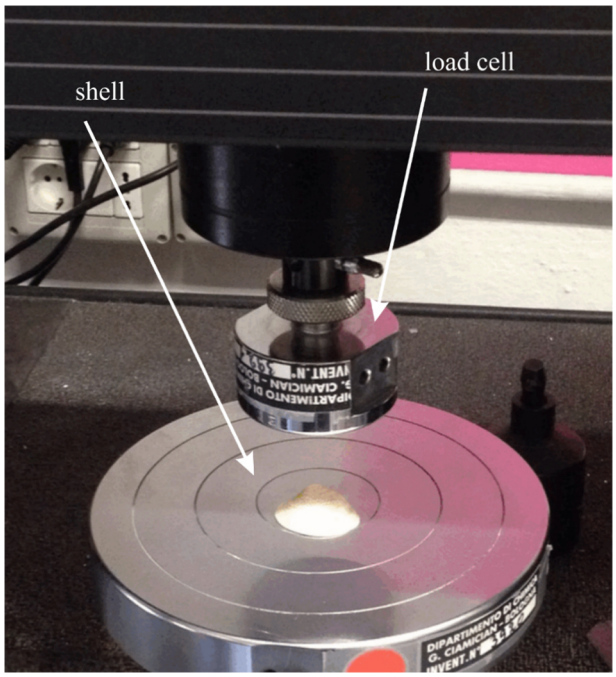

Fig. 4. Picture of the testing machine and setup used for the compression tests.

3. Analytical model

3.1. Description of the shell geometry

The valves present a very complex shape that can be described by four main quantities, as shown in Supplementary Fig. 2:

- the maximum Feret diameter f_{max}, i.e. the greatest lateral dimension;
- the minimum Feret diameter f_{min}, i.e. the smallest lateral dimension;
- the thickness h;
- the height of the centre of the shell z_0 from a horizontal plane.

For the purpose of the analytical model introduced later, it is

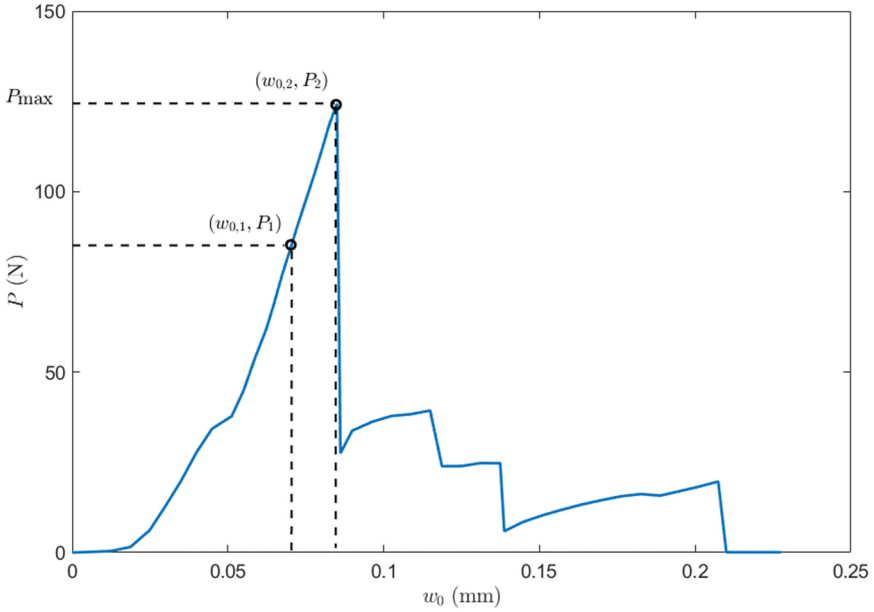

Fig. 5. Typical experimental load-displacement curve, with P the total load and w_0 the displacement of the centre of the shell from its natural position. (The two reference points on the linear segment will be used in Section 3 for the extraction of the Young's modulus.).

convenient to reduce the geometry described by the quantities above to an equivalent spherical cap. As schematised in Supplementary Fig. 3, the equivalent spherical cap can be considered as having the same height and thickness of the shell (i.e., z_0 and h, respectively) and a base radius R, which can be assumed to be:

$$R \approx \frac{f_{max} + f_{min}}{2} \tag{1}$$

The radius a of the equivalent sphere can be obtained from simple geometric considerations, i.e.:

$$a = \frac{z_0}{2} + \frac{R^2}{2z_0} \tag{2}$$

3.2. Extraction of the Young's modulus

Considering the experimental setup shown in Fig. 4 and the description of the geometry discussed above, we can approximate the system as a shallow spherical shell loaded over a small circular area of radius c, with centre at the apex and with no edge restraint (Reissner, 1946b; Timoshenko and Woinowsky-Krieger, 1959). The shallowness approximation consists in assuming that $R/a \ll 1$ (Reissner, 1946a). Strictly speaking, in our case this approximation is not perfectly fulfilled, because we have simply $R < a$ (and not $R \ll a$ as required) for almost all the samples, but we believe to obtain anyway a good description of the mechanical properties of the shells.

Let us consider the displacement at the centre of the loaded area, which is given by Timoshenko and Woinowsky-Krieger (1959):

$$w_0 = \frac{\sqrt{12(1-\nu^2)}}{\pi} \frac{Pa}{Eh^2} \left[\frac{1}{\mu^2} - \frac{\pi}{2\mu} \psi`_4(\mu) \right] \tag{3}$$

where ν is the Poisson's ratio, E the Young's modulus, ψ'_4 a tabulated function and μ the dimensionless coordinate:

$$\mu = \sqrt{12(1-\nu^2)} \frac{c}{\sqrt{ah}} \tag{4}$$

The radius c of the area of application of the load can be derived from the Hertz theory of contact. Considering the experimental setup and the shell geometry, we are in the case of a solid of revolution (i.e., the shell approximated by a spherical cap) in contact with a half-space (i.e., the steel platen through which the compressive load is applied). Thus, according to Johnson (1985):

$$c = \left(\frac{3Pa_{eq}}{4E_{eq}} \right)^{\frac{1}{3}} \tag{5}$$

where $a_{eq} = a$ and we can take $P = P_{max}$ and $E_{eq} = E$, given that the steel platen can be assumed to be rigid with respect to the shell. Strictly speaking, the Young's modulus to employ in the Hertz contact theory is that of a solid sphere, but the theory is still valid during the approach of the two solids, because the indentation depth is negligible with respect to the shell thickness. An analogous reasoning has already been applied in the literature (see, e.g., MansoorBaghaei and Sadegh, 2011 where the authors separate the elastic deformation of a spherical shell from the bending deflection).

By taking two reference points $(w_{0,1}, P_1)$ and $(w_{0,2}, P_2)$ on the linear segment of the experimental load-displacement curve, as shown in Fig. 5, the Young's modulus of the shell can be derived iteratively from Eq. (3) as:

$$E = \frac{\sqrt{12(1-\nu^2)}}{\pi} \frac{a}{h^2} \left[\frac{1}{\mu^2} - \frac{\pi}{2\mu} \psi`_4(\mu) \right] \frac{P_2 - P_1}{w_{0,2} - w_{0,1}} \tag{6}$$

where we can assume $\nu \approx 0.16$ for aragonite (Barthelat et al., 2006) and $E_{eq} = 30$ GPa as the initial value for the computation of c through Eq. (5) (see Supplementary Note 1 for details).

Table 2 reports the values of the Young's modulus, which falls in the order of 6 GPa, with the greatest E measured for the "CE" location. The

Table 2
Average value and standard deviation of the Young's modulus, from Eq. (6), and the ultimate strength, from Eq. (10), of the investigated samples ordered by decreasing latitudes.

Location acronym	E (GPa)	σ_u (MPa)
"MO"	2.44 ± 1.58	20.61 ± 3.74
"CH"	6.93 ± 1.57	33.41 ± 6.65
"GR"	6.18 ± 1.77	28.19 ± 5.77
"CE"	7.19 ± 2.19	34.38 ± 6.43
"SB"	6.94 ± 2.30	32.25 ± 8.65
"CA"	6.01 ± 3.88	28.68 ± 8.32

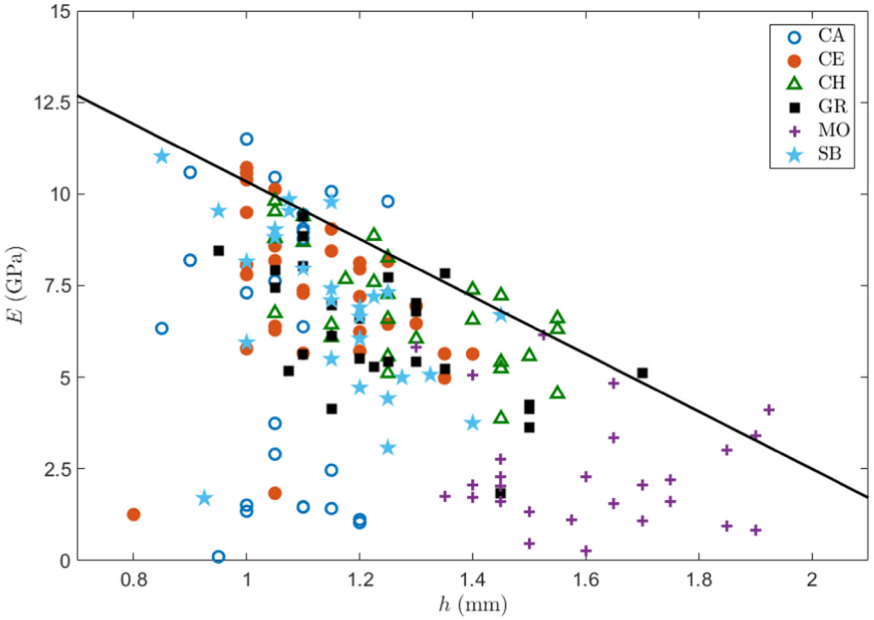

Fig. 6. Young's modulus, computed through Eq. (6), as function of the shell thickness of the investigated samples divided by location. The solid line represents the curve described by Eq. (7).

only exception is the "MO" location, whose shells present the biggest size and their load-displacement curves have a smaller stiffness and thus a smaller Young's modulus.

In Fig. 6 we plot the values of the Young's modulus for all the samples as function of the shell thickness: the general trend is that E diminishes for an increasing h. In addition, it is possible to identify a limiting curve that divides the plane in two parts. All the values are located below the curve, i.e., there are no shells with high thickness and simultaneously high Young's modulus. The limiting curve can be described by a best-fit of the type:

$$E(h) = A_1 + B_1 h \tag{7}$$

By taking the largest value of E for each thickness (see Supplementary Note 2 for details), we find $A_1 = 18.2$ GPa and $B_1 = -7.8$ GPamm^{-1}, with R^2-value 0.9185.

3.3. Extraction of the ultimate strength

Within the approximation of shallow spherical shells, the maximum bending stress can be computed as (Timoshenko and Woinowsky-Krieger, 1959):

$$\sigma_{b,\max} = \pm\frac{3(1+\nu)}{2}\frac{P_{\max}}{h^2}\frac{\psi'_3(\mu)}{\mu} \tag{8}$$

where ψ'_3 is another tabulated function, depending on the dimensionless coordinate introduced through Eq. (4), and is negative in the considered range of μ. Thus, in Eq. (8) we take the negative sign in order to have a positive maximum bending stress. The maximum membrane stress arising in the compressed shell, instead, is given by Timoshenko and Woinowsky-Krieger (1959):

$$\sigma_{m,\max} = \frac{\sqrt{12(1-\nu^2)}}{2\pi}\frac{P_{\max}}{h^2}\left[\frac{1}{\mu^2} - \frac{\pi}{2\mu}\psi'_4(\mu)\right] \tag{9}$$

and we take it as positive in the case of compression.

Finally, the ultimate strength of the shell σ_u is given by the sum of Eqs. (8) and (9), i.e.:

$$\sigma_u = \sigma_{b,\max} + \sigma_{m,\max} = -\frac{3(1+\nu)}{2}\frac{P_{\max}}{h^2}\frac{\psi'_3(\mu)}{\mu} + \frac{\sqrt{12(1-\nu^2)}}{2\pi}\frac{P_{\max}}{h^2}\left[\frac{1}{\mu^2} - \frac{\pi}{2\mu}\psi'_4(\mu)\right] \tag{10}$$

which, according to signs assumed above, is positive. Note that we get $\sigma_{m,\max} \ll \sigma_{b,\max}$ for all the samples, thus we can assume $\sigma_u \approx \sigma_{b,\max}$.

In the same Table 2, we list the ultimate strengths of all the tested shells computed through Eq. (10), obtaining values in the order of 30 MPa. As observed for the Young's modulus, also the ultimate strength depends slightly on the location, with the shells with a smaller E presenting also a smaller value of σ_u (i.e., "MO"). The relation among the Young's moduli of the shells from the different considered locations, is almost verified also for the ultimate strength, despite a larger scattering of the experimental data does not allow a precise discrimination.

As done before for the Young's modulus, in Fig. 7 we plot the computed ultimate strengths as function of the shell thickness, showing a similar decreasing trend of σ_u for increasing h. Again, we can divide the plane through a curve of equation:

$$\sigma_u(h) = A_2 + B_2 h \tag{11}$$

being A_2 and B_2 fitting parameters. By taking the largest value of σ_u for each thickness (see Supplementary Note 2 for details), we find $A_2 = 78.3$ MPa and $B_2 = -31.2$ MPamm^{-1}, with R^2-value 0.9090. The impossibility to have a simultaneous large thickness and large strength is typical of brittle materials, e.g. ceramics, as in the case of aragonite. For larger h, there is a larger probability to have defects (for instance, larger pores), which degrade the mechanical strength of the shells.

The values of the Young's modulus and the ultimate strength, computed through Eqs. (6) and (10) respectively, can be plotted on the two axes of a single graph, as we attempt to do in Fig. 8. In the obtained Ashby plot (Ashby, 1992) it is evident the large scattering of the experimental data, with the shells collected at the "MO" location occupying the bottom left corner, because of their small values of E and σ_u.

3.4. Effect of the shell porosity

As already observed in biological structural materials (Seto et al., 2012; Fantazzini et al., 2015), also *C. gallina* shells present a certain amount of porosity, which can affect the mechanical response and the fracture properties. In order to take into account the shell porosity, here denoted by the volume fraction φ, it is possible to rescale the computed values of E and σ_u according to the rules of mixtures employed for composite materials (Jones, 1999), respectively:

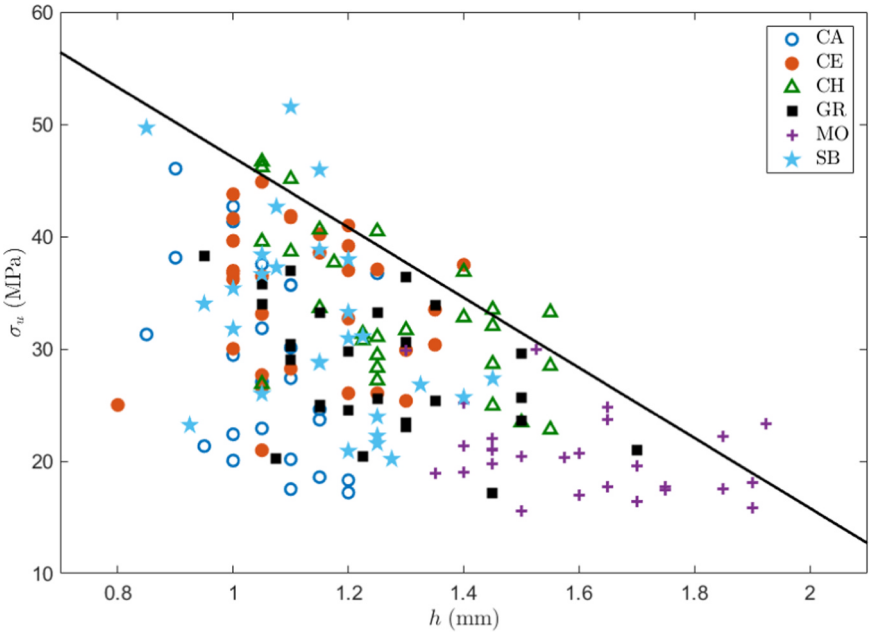

Fig. 7. Ultimate strength, computed through Eq. (10), as function of the shell thickness of the investigated samples divided by location. The solid line represents the curve described by Eq. (11).

$$E = E_{\text{mat}}(1-\varphi) + E_{\text{por}}\varphi \tag{12a}$$

$$\sigma_u = \sigma_{u,\text{mat}}(1-\varphi) + \sigma_{u,\text{por}}\varphi \tag{12b}$$

where E_{mat} and $\sigma_{u,\text{mat}}$ are the properties of the matrix, E_{por} and $\sigma_{u,\text{por}}$ the properties of the pores, and E and σ_u the macroscopic properties of the shell computed before. By assuming $E_{\text{por}} = 0$ GPa and $\sigma_{u,\text{por}} = 0$ MPa (i.e., there is no material in the pores), we can extract the actual properties of the matrix, i.e. the microscopic properties of the shells, as:

$$E_{\text{mat}} = \frac{E}{(1-\varphi)} \tag{13a}$$

$$\sigma_{u,\text{mat}} = \frac{\sigma_u}{(1-\varphi)} \tag{13b}$$

The values of E_{mat} and $\sigma_{u,\text{mat}}$ for all the samples are reported in Table 3, together with the average shell porosity. In general, we observe a slightly increasing porosity for a decreasing latitude and thus a larger effect on the mechanical properties of the shells. As the latitude decreases, the porosity generally increases and thus the difference between E and E_{mat}, and between σ_u and $\sigma_{u,\text{mat}}$, increases. Anyway, being φ always in the range $2 \div 5\%$, the difference between the mechanical properties computed through Eqs. (6,10), and reported in Table 2, and those obtained by considering the porosity through Eqs. (13a,13b), is always below 5%.

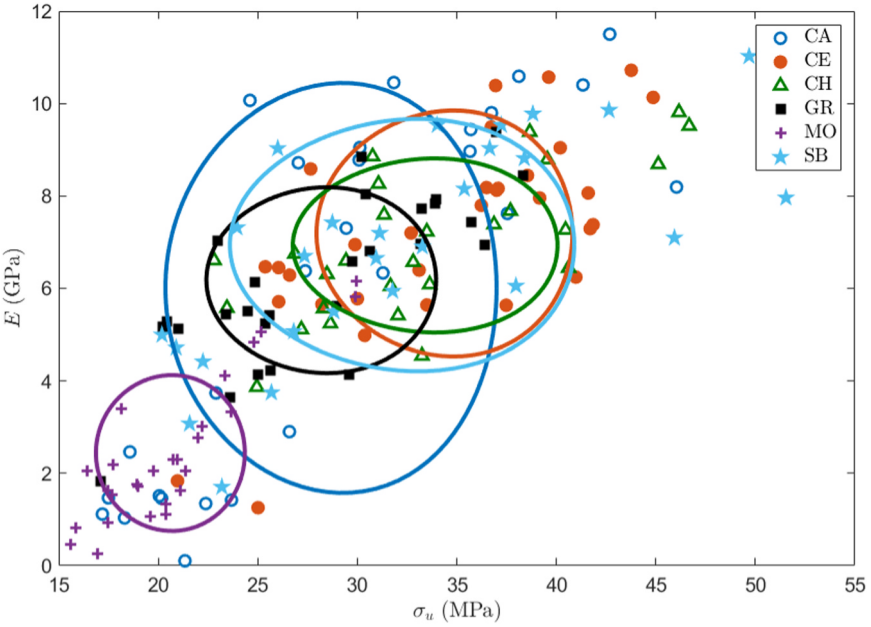

Fig. 8. Ashby plot of the Young's modulus and the ultimate strength of the investigated samples divided by location. Each ellipse has centre in ($\sigma_{u,m}$, E_m) and horizontal and vertical semi-axes $\sigma_{u,std}$ and E_{std}, respectively. The subscripts "m" and "std" denote the average value and the standard deviation, respectively, of the considered quantity as reported in Table 2.

Table 3
Average value and standard deviation of the Young's modulus, from Eq. (13a), and the ultimate strength, from Eq. (13b), of the investigated samples ordered by decreasing latitudes, considering the shell porosity.

Location acronym	φ (%)	E_{mat} (GPa)	$\sigma_{u,mat}$ (MPa)
"MO"	2.97 ± 0.48	2.51 ± 1.63	21.24 ± 3.86
"CH"	2.97 ± 0.69	7.15 ± 1.62	34.42 ± 6.76
"GR"	3.85 ± 0.79	6.43 ± 1.83	29.32 ± 6.00
"CE"	3.97 ± 1.01	7.48 ± 2.27	34.75 ± 6.35
"SB"	3.71 ± 0.88	7.20 ± 2.38	33.51 ± 9.04
"CA"	4.03 ± 0.90	6.26 ± 4.04	29.88 ± 8.61

3.5. Extraction of the toughness modulus and fracture energy

Here we attempt to extract the energy dissipated from the fracture of the *C. gallina* valves, assuming that each shell breaks into two parts and the fracture involves the entire cross section in Fig. 1. The fracture pattern could be also very complex involving the rupture in multiple pieces. However, the main objective here is to discriminate between the properties of the inner and the outer layer, defining nominal/effective rather than real/complex mechanical properties.

Considering Fig. 5, we define the total dissipated energy U_{TOT} as the area below the force-displacement curve, i.e.:

$$U_{TOT} = \int_0^{w_{0,\max}} P(w_0)\mathrm{d}w_0 = \sum_{i=1}^{N} \int_0^{w_{0,i}} P_i(w_0)\mathrm{d}w_0 \tag{14}$$

being $w_{0,\max}$ the fracture displacement and we have introduced the summation because the overall curve can be approximated by a piecewise function of N continuous functions. Thus, we can define the total toughness modulus as:

$$T_{TOT} = \frac{U_{TOT}}{V} = \frac{1}{V}\int_0^{w_{0,\max}} P(w_0)\mathrm{d}w_0 = \frac{1}{V}\sum_{i=1}^{N} \int_0^{w_{0,i}} P_i(w_0)\mathrm{d}w_0 \tag{15}$$

where V is the volume of the shell, taken as the average between the right and left valve of each sample.

The fracture energy, instead, is defined with reference to the fracture area A, which here we can assume equal to the cross section of the shell (see Fig. 1 and Supplementary Fig. 3), i.e.:

$$G_{c,TOT} = \frac{U_{TOT}}{A} = \frac{1}{A}\int_0^{w_{0,\max}} P(w_0)\mathrm{d}w_0 = \frac{1}{A}\sum_{i=1}^{N} \int_0^{w_{0,i}} P_i(w_0)\mathrm{d}w_0 \tag{16}$$

As anticipated above, we can assume that the internal layer of the shell is the first one that undergoes fracture, followed by the external layer. Therefore, if from Fig. 5 we assume that the peak of the force is reached when the internal layer fails, we can easily compute the toughness modulus of the internal layer (T_{int}) and that of the external layer (T_{ext}) of the shell. The integral in Eq. (15), consequently, must be divided into two parts:

$$T_{int} = \frac{1}{V_{int}}\int_0^{w_0|_{P_{\max}}} P(w_0)\mathrm{d}w_0 \tag{17a}$$

$$T_{ext} = \frac{1}{V_{ext}}\int_{w_0|_{P_{\max}}}^{w_{0,\max}} P(w_0)\mathrm{d}w_0 \tag{17b}$$

being $w_0|_{P_{\max}}$ the displacement at which the maximum load occurs and V_{int} and V_{ext} the volumes of the internal and the external layers, respectively.

Similarly, we can compute the fracture energy of the internal and the external layer, by dividing the corresponding integral in Eq. (16) as done above for the toughness modulus, i.e.:

$$G_{c,int} = \frac{1}{A_{int}}\int_0^{w_0|_{P_{\max}}} P(w_0)\mathrm{d}w_0 \tag{18a}$$

Table 4
Average value and standard deviation of the toughness modulus and the fracture energy of the internal and the external layers of the investigated samples ordered by decreasing latitudes.

Location acronym	Internal layer		External layer	
	T_{int} (kJ/m^3)	$G_{c,int}$ (kJ/m^2)	T_{ext} (kJ/m^3)	$G_{c,ext}$ (kJ/m^2)
"MO"	12.32 ± 2.92	0.20 ± 0.05	8.34 ± 4.26	0.13 ± 0.07
"CH"	16.30 ± 6.14	0.27 ± 0.10	6.98 ± 3.78	0.11 ± 0.06
"GR"	11.06 ± 4.54	0.18 ± 0.07	8.86 ± 3.92	0.14 ± 0.06
"CE"	14.96 ± 4.28	0.26 ± 0.08	7.32 ± 4.44	0.12 ± 0.08
"SB"	13.44 ± 6.38	0.23 ± 0.12	10.52 ± 6.10	0.17 ± 0.10
"CA"	11.64 ± 4.54	0.19 ± 0.07	9.80 ± 7.38	0.16 ± 0.12

$$G_{c,ext} = \frac{1}{A_{ext}}\int_{w_0|_{P_{\max}}}^{w_{0,\max}} P(w_0)\mathrm{d}w_0 \tag{18b}$$

Given the availability of the actual volume V of the shells, measured experimentally as described before, for the values of V_{int} and V_{ext} we do not make use of the spherical shape approximation introduced earlier for the computation of the mechanical properties. Instead, we notice that $V_{int} \approx V_{ext} \approx V/2$, thus we use the experimental value $V/2$ for the extraction of the toughness moduli in Eq. (17). Note also that we have introduced the fracture areas of the internal and the external layers, A_{int} and A_{ext} respectively, assuming that each layer covers half of the cross section (see Fig. 2a), i.e. the thickness of the internal layer is assumed equal to the thickness of the external layer, and using the spherical shape approximation. See Supplementary Note 3 for the detailed computation of A_{int}, A_{ext}, V_{int} and V_{ext}.

In Table 4 we list the computed values of toughness modulus and fracture energy for the internal and external layers of all the samples. It is difficult to observe a clear dependence of these quantities on the location (i.e. latitude) of collection of the samples, but interestingly the sums $T_{int} + T_{ext}$ and $G_{c,int} + G_{c,ext}$ are almost the same for every location. On the other hand, a strong difference between the two layers can be observed: the internal layer presents always much larger toughness moduli and fracture energies.

4. Conclusions

We have presented an experimental investigations of *Chamelea gallina* shells, collected at different locations in the Adriatic Sea. Microscopy investigations on the cross section of the shells have highlighted the presence of two main layers with different microstructures, which interact with the propagation of cracks during mechanical loading.

Compression tests have been performed to extract the main mechanical properties of the shells, namely Young's modulus and ultimate strength, which have been derived through an analytical model based on the shallow spherical shell approximation. Results have shown a certain dependency of the mechanical performance on the latitude of collection of the samples, and these findings are essentially preserved when the shell porosity is considered. These results confirm that the preliminary outcomes of a previous work (Gizzi et al., 2016), for a variety of physical properties, are consistent also for the mechanical properties of the shells. The latitudinal gradient has been demonstrated to not affect significantly the internal microstructure of the shells, but only their macroscale morphology. Thus, we can conclude that the values of the Young's modulus and the ultimate strength depend on the latitude due to the change in shell morphology (e.g. thickness). Finally, we have investigated the fracture properties of the considered shells, which present a complex fracture growth as usually observed in natural and artificial composites. We have computed the toughness modulus and the fracture energy for the two layers (i.e. internal and external) that fail progressively under compression: the extracted properties are

nearly independent from the latitude, but highlight a different mechanical behaviour of the two layers, with the internal one being able of absorbing more energy at fracture.

Our findings can be of interest for the estimation of the future yield of the clam fisheries in the Adriatic Sea, by correlating the mechanical properties of the shells to e.g. the mortality events. From the mechanical point of view, instead, the measured properties can be of relevance for the design and optimization of new bio-inspired composite materials (Libonati et al., 2016; Gu et al., 2017; Pugno and Valentini, 2019), e.g. multilayer composites for shell structures.

Acknowledgements

NMP is supported by the European Commission under the Graphene Flagship Core 2 Grant no. 785219 (WP14 “Composites”) and FET Proactive “Neurofibres” Grant no. 732344 as well as by the Italian Ministry of Education, University and Research (MIUR) under the “Departments of Excellence” Grant L.232/2016 and ARS01-01384-PROSCAN Grant. RG is supported by the European Commission under the FET Proactive “Neurofibres” Grant no. 732344.

Appendix A. Supplementary material

Supplementary data associated with this article can be found in the online version at doi:10.1016/j.jmbbm.2019.02.032.

References

Ashby, M.F., 1992. Materials Selection in Mechanical Design. Pergamon Press, Oxford.
Barthelat, F., Li, C.M., Comi, C., Espinosa, H.D., 2006. Mechanical properties of nacre constituents and their impact on the mechanical performance. J. Mater. Res. 21, 1977–1986. https://doi.org/10.1557/jmr.2006.0239.
Barthelat, F., Rim, J., Espinosa, H.D., 2009. A review on the mechanical properties of mollusk shells - Perspectives on synthetic biomimetic materials. In: Bhushan, B., Fuchs, H. (Eds.), Applied Scanning Probe Methods XIII: Biomimetics and Industrial Applications. Springer-Verlag, Berlin.
Barthelat, F., Yin, Z., Buehler, M.J., 2016. Structure and mechanics of interfaces in biological materials. Nat. Rev. Mat. 1, 16007. https://doi.org/10.1038/natrevmats.2016.7/.
Bignardi, C., Petraroli, M., Pugno, N.M., 2010. Nanoindentations on conch shells of gastropoda and bivalvia molluscs reveal anisotropic evolution against external attacks. J. Nanosci. Nanotechnol. 10, 6453–6460. https://doi.org/10.1166/jnn.2010.2626.
DeWitt, T.J., Scheiner, S.M., 2004. Phenotypic Plasticity: Functional and Conceptual Approaches. Oxford University Press, Oxford.
Espinosa, H.D., Juster, A.L., Latourte, F.J., Loh, O.Y., Gregoire, D., Zavattieri, P.D., 2011. Tablet-level origin of toughening in abalone shells and translation to synthetic composite materials. Nat. Commun. 2, 173. https://doi.org/10.1038/ncomms1172.
Fantazzini, P., Mengoli, S., Pasquini, L., Bortolotti, V., Brizi, L., Mariani, M., Di Giosia, M., Fermani, S., Capaccioni, B., Caroselli, E., Prada, F., Zaccanti, F., Levy, O., Dubinsky, Z., Kaandorp, J.A., Konglerd, P., Hammel, J.U., Dauphin, Y., Cuif, J.P., Weaver, J.C., Fabricius, K.E., Wagermeier, W., Fratzl, P., Falini, G., Goffredo, S., 2015. Gains and losses of coral skeletal porosity changes with ocean acidification acclimation. Nat. Commun. 6, 7785. https://doi.org/10.1038/ncomms8785.
Gilbert, S.F., 2001. Ecological developmental biology: developmental biology meets the real world. Dev. Biol. 233, 1–12. https://doi.org/10.1006/dbio.2001.0210.
Gizzi, F., Caccia, M.G., Simoncini, G.A., Mancuso, A., Reggi, M., Fermani, S., Brizi, L., Fantazzini, P., Stagioni, M., Falini, G., Piccinetti, C., Goffredo, S., 2016. Shell properties of commercial clam Chamelea gallina are influenced by temperature and solar radiation along a wide latitudinal gradient. Sci. Rep. 6, 36420. https://doi.org/10.1038/srep36420.
Gu, G.X., Takaffoli, M., Buehler, M.J., 2017. Hierarchically enhanced impact resistance of bioinspired composites. Adv. Mater. 29, 1700060.
Huang, Z., Li, X., 2009. Nanoscale structural and mechanical characterization of heat treated nacre. Mat. Sci. Eng. C 29, 1803–1807. https://doi.org/10.1016/j.msec.2009.02.007.
Huang, Z., Li, X., 2013. Origin of flaw-tolerance in nacre. Sci. Rep. 3, 1693. https://doi.org/10.1038/srep01693.
Ji, H., Li, X., Chen, D., 2017. *Cymbiola nobilis* shell: toughening mechanisms in a crossed-lamellar structure. Sci. Rep. 7, 40043. https://doi.org/10.1038/srep40043.
Johnson, K.L., 1985. Contact Mechanics. Cambridge University Press, Cambridge.
Jones, R.M., 1999. Mechanics of Composite Materials. Taylor & Francis, London.
Kakisawa, H., Sumitomo, T., 2011. The toughening mechanism of nacre and structural materials inspired by nacre. Sci. Technol. Adv. Mater. 12, 064710. https://doi.org/10.1088/1468-6996/12/6/064710.
Keller, L., Rask, J., Buseck, P., 1989. JCPDS card no. 41-1475. Arizona State Univ., Tempe, AZ, USA., ICDD Grant-in-Aid.
Li, H., Jin, D., Li, R., Li, X., 2015. Structural and mechanical characterization of thermally treated conch shells. JOM 67, 720–725. https://doi.org/10.1007/s11837-015-1330-y.
Li, H., Xu, Z.H., Li, X., 2013. Multiscale hierarchical assembly strategy and mechanical prowess in conch shells (*Busycon carica*). J. Struct. Biol. 184, 409–416. https://doi.org/10.1016/j.jsb.2013.10.011.
Li, X., Chang, W.C., Chao, Y.J., Wang, R., Chang, M., 2004. Nanoscale structural and mechanical characterization of a natural nanocomposite material: the shell of red abalone. Nano Lett. 4, 613–617. https://doi.org/10.1021/nl049962k.
Li, X., Nardi, P., 2004. Micro/nanomechanical characterization of a natural nanocomposite material - the shell of Pectinidae. Nanotechnology 15, 211–217. https://doi.org/10.1088/0957-4484/15/1/038.
Libonati, F., Gu, G.X., Zhao, Q., Vergani, L., Buehler, M.J., 2016. Bone-inspired materials by design: toughness amplification observed using 3D printing and testing. Adv. Eng. Mater. 18, 1354–1363. https://doi.org/10.1002/adem.201600143.
Lowenstam, H.A., Weiner, S., 1989. On Biomineralization. Oxford University Press, Oxford.
MansoorBaghaei, S., Sadegh, A.M., 2011. Elastic spherical shell impacted with an elastic barrier: a closed form solution. Int. J. Solids Struct. 48, 3257–3266. https://doi.org/10.1016/j.ijsolstr.2011.07.016.
Mayer, G., 2017. Mechanical energy dissipation in natural ceramic composites. J. Mech. Behav. Biomed. 76, 21–29. https://doi.org/10.1016/j.jmbbm.2017.06.019.
Matozzo, V., Marin, M.G., 2011. Bivalve immune responses and climate changes: is there a relationship? Invertebr. Surviv. J. 8, 70–77.
Melatunan, S., Calosi, P., Rundle, S.D., Widdicombe, S., Moody, A.J., 2013. Effects of ocean acidification and elevated temperature on shell plasticity and its energetic basis in an intertidal gastropod. Mar. Ecol. Prog. Ser. 472, 155–168. https://doi.org/10.3354/meps10046.
Mohanty, B., Katti, K.S., Katti, D.R., Verma, D., 2006. Dynamic nanomechanical response of nacre. J. Mater. Res. 21, 2045–2051. https://doi.org/10.1557/jmr.2006.0247.
Moschino, V., Marin, M.G., 2006. Seasonal changes in physiological responses and evaluation of “well-being” in the Venus clam Chamelea gallina from the Northern Adriatic Sea. Comp. Biochem. Phys. A 145, 433–440. https://doi.org/10.1016/j.cbpa.2006.07.021.
Pilati, T., Demartin, F., Gramaccioli, C.M., 1998. Lattice-dynamical estimation of atomic displacement parameters in carbonates: calcite and aragonite $CaCO_3$, dolomite $CaMg(CO_3)_2$ and magnesite $MgCO_3$. Acta Crystallogr. B 54, 515–523. https://doi.org/10.1107/S0108768197018181.
Popov, S.V., 1986. Composite prismatic structure in bivalve shells. Acta Palaeontol. Pol. 31, 3–26.
Pugno, N.M., Valentini, L., 2019. Bionicomposites. Nanoscale 11, 3102–3111. https://doi.org/10.1039/c8nr08569b.
Ramón, M., Richardson, C.A., 1992. Age determination and shell growth of Chamelea gallina (Bivalvia: veneridae) in the western Mediterranean. Mar. Ecol. Prog. Ser. 89, 15–23.
Reissner, E., 1946a. Stresses and small displacements of shallow spherical shells. I. J. Math. Phys. Camb. 25, 80–85. https://doi.org/10.1002/sapm194625180.
Reissner, E., 1946b. Stresses and small displacements of shallow spherical shells. II. J. Math. Phys. Camb. 25, 279–300. https://doi.org/10.1002/sapm1946251279.
Romanelli, M., Cordisco, C.A., Giovanardi, O., 2008. The long term decline of the Chamelea gallina L. (Bivalvia: veneridae) clam fishery in the Adriatic Sea: is a synthesis possible? Acta Adriat. 50, 171–205.
Seto, J., Ma, Y., Davis, S.A., Meldrum, F., Gourrier, A., Kim, Y.Y., Schilde, U., Sztucki, M., Burghammer, M., Maltsev, S., Jäger, C., 2012. Structure-property relationships of a biological mesocrystal in the adult sea urchin spine. P. Natl. Acad. Sci. USA 109, 3699–3704. https://doi.org/10.1073/pnas.1109243109.
Sun, J., Bhushan, B., 2012. Hierarchical structure and mechanical properties of nacre: a review. RSC Adv. 2, 7617–7632. https://doi.org/10.1039/C2RA20218B.
Taylor, J.D., Layman, M., 1972. The mechanical properties of bivalve (Mollusca) shell structures. Palaeontology 15, 73–87.
Timoshenko, S., Woinowsky-Krieger, S., 1959. Theory of Plates and Shells. McGraw-Hill, New York.
Watson, S.A., Peck, L.S., Tyler, P.A., Southgate, P.C., Tan, K.S., Day, R.W., Morley, S.A., 2012. Marine invertebrate skeleton size varies with latitude, temperature and carbonate saturation: implications for global change and ocean acidification. Glob. Change Biol. 18, 3026–3038. https://doi.org/10.1111/j.1365-2486.2012.02755.x.
Xu, Z.H., Li, X., 2011. Deformation strengthening of biopolymer in nacre. Adv. Funct. Mater. 21, 3883–3888. https://doi.org/10.1002/adfm.201100167.
Yuan, Q., Chen, B., Chen, B., Wang, Z., 2016. New insight into the toughening mechanisms of seashell: from arch shape to multilayer structure. J. Nanomater. 2016, 3817985. https://doi.org/10.1155/2016/3817985.

Supplementary Information

Mechanical properties of *Chamelea gallina* shells

Roberto Guarino[1], Stefano Goffredo[2,3], Giuseppe Falini[4], Nicola Maria Pugno[1,5,6,*]

[1] *Laboratory of Bio-Inspired & Graphene Nanomechanics, Department of Civil, Environmental and Mechanical Engineering, University of Trento, Via Mesiano 77, 38123 Trento, Italy*

[2] *Marine Science Group, Department of Biological, Geological and Environmental Sciences, University of Bologna, Via F. Selmi 3, 40126 Bologna, Italy*

[3] *Laboratory of Marine Biology and Fisheries at Fano, Department of Biological, Geological and Environmental Sciences, University of Bologna, Viale Adriatico 1/N, 61032 Fano, Italy*

[4] *Department of Chemistry 'Giacomo Ciamician', University of Bologna, Via F. Selmi 2, 40126 Bologna, Italy*

[5] *Ket Lab, Edoardo Amaldi Foundation, Via del Politecnico snc, 00133 Rome, Italy*

[6] *School of Engineering and Materials Science, Queen Mary University of London, Mile End Road, E1-4NS London, United Kingdom*

***** *Corresponding author: nicola.pugno@unitn.it*

Supplementary Figure 1

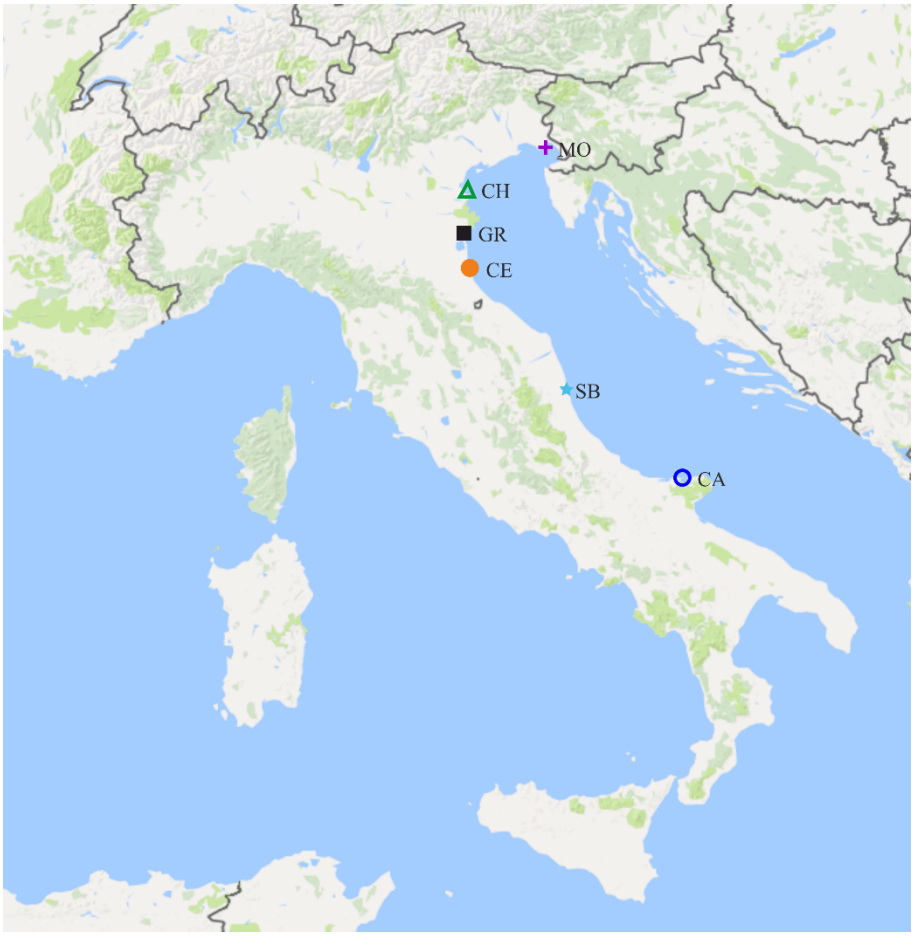

Figure S1 Map of Italy and selected locations for the collection of the samples. The map has been generated from http://maps.google.com (Google Inc., United States of America).

Supplementary Figure 2

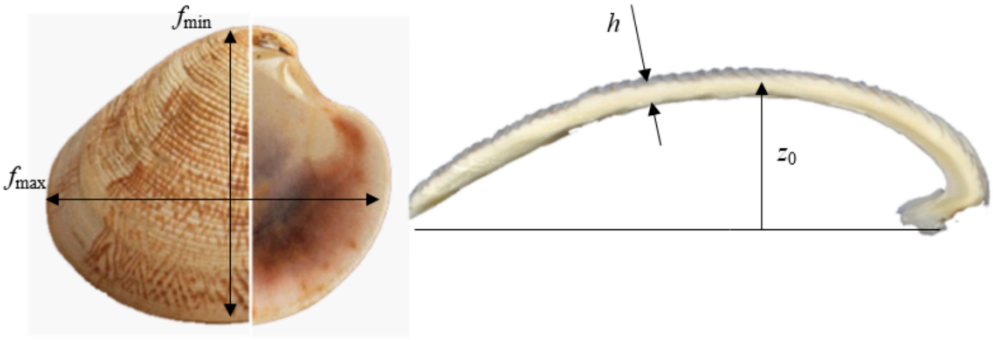

Figure S2 Main geometrical quantities for the description of a clam shell, adapted from Figure 1.

Supplementary Figure 3

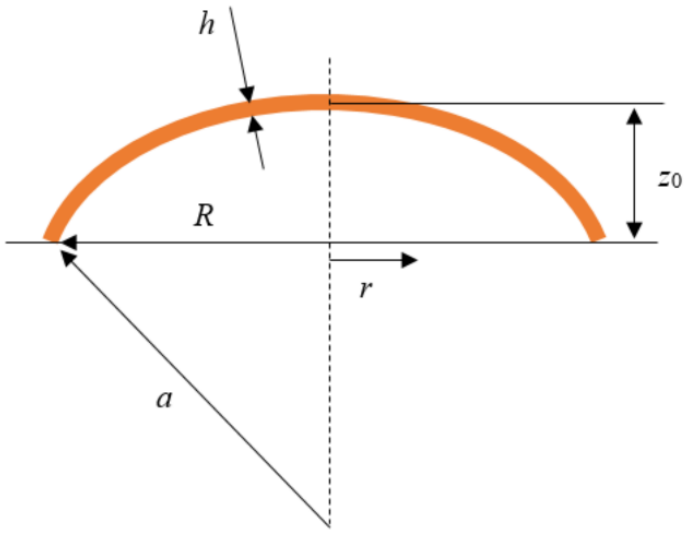

Figure S3 Equivalent spherical cap geometry and main quantities, with $0 \leq r \leq R$ the radial coordinate.

Supplementary Note 1

Choice of the initial value of the Young's modulus

The use of Equations (5), (4) and (6), in the order, for the estimation of the Young's modulus of the shells, should follow an iterative procedure. However, given the uncertainties introduced through the numerical function ψ'_4 and the computation of the slope of the experimental load-displacement curves, we believe to obtain a good approximation of E by assuming only one initial value.

We carry out a convergence study considering different initial values of E and the results are reported in Table S1, for the example case of the "CA" location. As specified in the text, we observe that $E = 30$ GPa represents a good initial guess since for larger values the final result does not change significantly.

Table S1 Initial guess for the Young's modulus and corresponding computed value through Equations (5), (4) and (6), in the order. Example computation for all the samples collected at the "CA" location.

initial *E* (GPa)	**computed *E*** (GPa)
10	4.80 ± 3.01
15	5.13 ± 3.22
20	5.44 ± 3.51
25	5.60 ± 3.46
30	6.01 ± 3.88
35	5.89 ± 3.77
40	5.95 ± 3.71
45	5.68 ± 3.83
50	6.01 ± 4.23

Supplementary Note 2

Details on the best-fits through Equations (7) and (11)

Equation (7) is applied as best-fit on the largest values of E for each value of thickness. Specifically, the considered thicknesses are from 0.85 to 1.90 mm, with 0.05 mm steps. The values of E corresponding to h = 1.60, 1.75 and 1.80 mm are not taken into account, for the lack of valuable data.

Equation (11) is applied as best-fit on the largest values of σ_u for each value of thickness. Specifically, the considered thicknesses are from 0.85 to 1.90 mm, with 0.05 mm steps. The values of σ_u corresponding to h = 0.95, 1.60, 1.75 and 1.80 mm are not taken into account, for the lack of valuable data.

Supplementary Note 3

Details on the computation of the fracture areas in Equations (18)

For the computation of the fracture areas A_{int} and A_{ext}, since no experimental data are available, we consider the approximated spherical shape shown in Figure S3. Assuming that each layer covers half of the thickness, the corresponding cross sections are given by:

$$A_{ext} = \frac{\pi\,\alpha}{180}\frac{\left(a+\frac{h}{2}\right)^2 - a^2}{2}$$

$$A_{int} = \frac{\pi\,\alpha}{180}\frac{a^2 - \left(a-\frac{h}{2}\right)^2}{2}$$

for the external and the internal layer, respectively. The quantities a and h are shown in Figure S3, while the angle α is given by:

$$\alpha = 2\ \sin^{-1}\left(\frac{R}{a}\right)$$

Similarly, the volume of the internal and the external layers, considering the spherical shape approximation in Figure S3, are given by, respectively:

$$V_{ext} = \pi\left(z_0+\frac{h}{2}\right)^2\left[a-\frac{1}{3}\left(z_0+\frac{h}{2}\right)\right] - \pi {z_0}^2\left(a-\frac{1}{3}z_0\right)$$

$$V_{int} = \pi {z_0}^2\left(a-\frac{1}{3}z_0\right) - \pi\left(z_0-\frac{h}{2}\right)^2\left[a-\frac{1}{3}\left(z_0-\frac{h}{2}\right)\right]$$

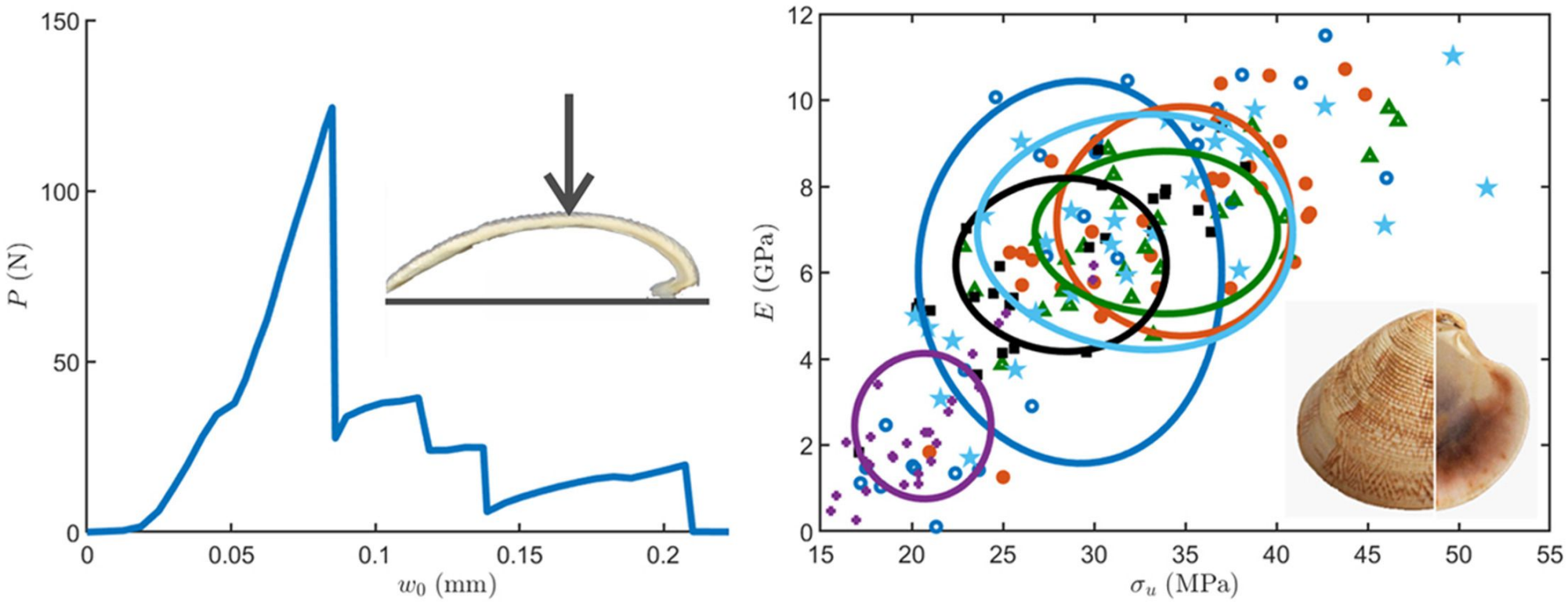
150
100
50
0
P (N)
0
0.05
0.1
0.15
0.2
w_0 (mm)
12
10
8
6
4
2
0
E (GPa)
15
20
25
30
35
40
45
50
55
σ_u (MPa)